Thin Solid Films 578 (2015) 133–138

Contents lists available at ScienceDirect

Thin Solid Films

journal homepage: www.elsevier.com/locate/tsf

Thermal conductivity of titanium nitride/titanium aluminum nitride multilayer coatings deposited by lateral rotating cathode arc

M.K. Samani [a,b,f,*], X.Z. Ding [b], N. Khosravian [f], B. Amin-Ahmadi [c], Yang Yi [d], G. Chen [e], E.C. Neyts [f], A. Bogaerts [f], B.K. Tay [a]

[a] Novitas, Nanoelectronics Centre of Excellence, School of Electrical & Electronic Engineering, Nanyang Technological University, Singapore 639798, Singapore
[b] Surface Technology Group, Singapore Institute of Manufacturing Technology, 71 Nanyang Drive, Singapore 638075, Singapore
[c] Electron Microscopy for materials Science (EMAT), Department of Physics, University of Antwerpen, Groenenborgerlan 171, B-2020 Antwerpen, Belgium
[d] Data Storage Institute, A*STAR (Agency for Science, Technology and Research), 117608, Singapore
[e] BC Photonics Technological Company, 5255 Woodwards Rd., Richmond, BC V7E 1G9, Canada
[f] Research Group PLASMANT, Department of Chemistry, University of Antwerp, Universiteitsplein 1, B-2610 Antwerp, Belgium

ARTICLE INFO

Article history:
Received 7 August 2014
Received in revised form 16 January 2015
Accepted 12 February 2015
Available online 21 February 2015

Keywords:
Thermal conductivity
Titanium nitride
Titanium aluminum nitride
Multilayer coatings
Pulsed photothermal reflectance technique

ABSTRACT

A series of $[TiN/TiAlN]_n$ multilayer coatings with different bilayer numbers $n = 5, 10, 25, 50$, and 100 were deposited on stainless steel substrate AISI 304 by a lateral rotating cathode arc technique in a flowing nitrogen atmosphere. The composition and microstructure of the coatings have been analyzed by using energy dispersive X-ray spectroscopy, X-ray diffraction (XRD), and conventional and high-resolution transmission electron microscopy (HRTEM). XRD analysis shows that the preferential orientation growth along the (111) direction is reduced in the multilayer coatings. TEM analysis reveals that the grain size of the coatings decreases with increasing bilayer number. HRTEM imaging of the multilayer coatings shows a high density misfit dislocation between the TiN and TiAlN layers. The cross-plane thermal conductivity of the coatings was measured by a pulsed photothermal reflectance technique. With increasing bilayer number, the multilayer coatings' thermal conductivity decreases gradually. This reduction of thermal conductivity can be ascribed to increased phonon scattering due to the disruption of columnar structure, reduced preferential orientation, decreased grain size of the coatings and present misfit dislocations at the interfaces.

1. Introduction

In order to improve the performance and service life of cutting and forming tools, nitrides of binary metal alloy coatings are coated on them resulting in a higher hardness and toughness. Ti-based hard coatings (e.g. TiN and TiAlN) are well known hard coatings in industry applications, typically deposited by physical vapor deposition [1,2]. TiAlN shows excellent mechanical properties, such as high hardness, oxidation resistance and excellent thermal stability [3,4]. Controlled deposition of the thin film allows producing multilayer materials with unique mechanical and physical properties. Knutsson et al. reported that the hardness of TiAlN/TiN multilayer coatings was higher than the single layer and increases with decreasing multilayer period [5]. It has been shown that multilayer TiN/TiAlN coatings are superior to single layer TiN and TiAlN coatings in many mechanical properties [6].

Besides the protection requirement against wear and oxidation, the thermal properties, and especially the thermal conductivity of hard coatings play an important role in their performance. For instance, materials with high thermal conductivity are required for electronic devices in order to dissipate heat, and act as a heat sink. Materials with low thermal conductivity are required for hard coatings and barrier coated elements in order to reduce the heat transport from the hot to the cold sides, and act as heat insulation. In high-speed machining, hot forging and casting, the temperature at the tool–chip interface moves up and this affects various tooling parameters (e.g. materials softening [7], friction condition and tool deformation [8]) and coating formation and properties (e.g. oxidation rate, hardness and thermal conductivity). A lower thermal conductivity of the hard coating is desired as a barrier layer to delay the temperature rising on the tool substrate materials and redirects heat flow into the chip and to dissipate the heat from the chip. This effect helps to reduce heat transport to the metallic components and thereby protects the tools against thermal overload [9–11]. Recently, it was reported that nano-multilayered TiAlN/Cu coatings have better cutting performance due to the lower thermal conductivity of nano-multilayered AlTiN/Cu than single layer TiAlN [12].

In our previous works [13,14], room temperature thermal conductivity values of a series of TiAlN coatings with a different Al/Ti atomic ratio and TiAlSiN nanocomposite coatings with different (Al + Si)/Ti atomic ratios on an AISI 304 substrate have been measured by pulsed

* Corresponding author at: Novitas, Nanoelectronics Centre of Excellence,Singapore, School of Electrical & Electronic Engineering, Nanyang Technological University, Singapore 639798, Singapore.
E-mail address: majid1@e.ntu.edu.sg (M.K. Samani).

http://dx.doi.org/10.1016/j.tsf.2015.02.032
0040-6090/

Table 1
Ti and Al content in the TiN and TiAlN layers in the multilayer coatings.

Layer	Ti content (at.%)	Al content (at.%)
TiN	44.8 ± 2.8	–
TiAlN	20.5 ± 2.7	30.4 ± 3.0

photothermal reflectance technique (PPR). The results showed that the thermal conductivity of the TiN coatings decreases rapidly with Al incorporation and also it was found that the nanocomposite TiAlSiN coatings' thermal conductivity decreases with increasing (Al + Si)/Ti atomic ratio. In the present work, we investigate the thermal conductivity of TiN/TiAlN multilayer coatings, and demonstrate that it is lower than the thermal conductivity of TiN and TiAlN coatings. Moreover, it will be shown that the thermal conductivity depends on the coatings' microstructure and number of layers.

2. Experimental methods

$[TiN/TiAlN]_n$ multilayer coatings with a thickness of about 1.2 μm were grown onto a mirror-finished AISI 304 stainless steel substrate (with a dimension of 25 × 25 × 1 mm^3 and surface roughness of 10 nm) using a lateral rotating cathode arc (LARC) technique, which has been described in detail elsewhere [15]. For deposition of the multi-layer coatings, one elemental Ti and Al cathodes were employed in this work. These two cathodes are laterally rotating during the coating deposition. At first, the substrates were ultrasonically cleaned in a series of alkaline solutions, washed in deionized water, and dried by nitrogen gas blowing and further dried in an oven at 100 °C. Then the precleaned substrates were mounted on a carrousel substrate holder which rotated continuously around the vertical central axis at a speed of 12 rpm. The coating deposition was conducted in a flowing pure nitrogen atmosphere with a working pressure controlled at 1.5 Pa. During the deposition, a negative bias of −70 V was applied to the substrate, and the substrate temperature was controlled at 480 °C. In order to control the composition of the as-deposited coatings, the direct current applied on the two cathodes, I_{Al} and I_{Ti} was fixed at 120 A and 50 A, respectively. For depositing the $[TiAlN/TiN]_n$ multilayer coatings, the DC current applied on the Al cathode was turned on and off periodically. The total deposition time is fixed at 60 min, and the time to deposit each layer is 30/*n* min. We have prepared a series of five $[TiN/TiAlN]_n$ multilayer coatings with bilayer number *n* equal to 5, 10, 25, 50, and 100. The corresponding bilayer thickness ranges then from about 240 nm to 12 nm. Two TiN and TiAlN single layer coatings were deposited under identical conditions on the AISI 304 substrate as well. The DC current of the Al cathode I_{Al} for TiN deposition was fixed at 0 A.

The crystalline structure of the coatings is analyzed by X-ray diffraction (XRD). The XRD measurements were performed on a Burker AXS D8 Advance X-ray diffractometer by using a Cu Kα radiation (λ = 1.54178 Å, 40 kV, 40 mA) under θ–2θ scan mode in a 2θ range from 30° to 80°.

Sample preparation for cross sectional transmission electron microscopy (TEM) and scanning transmission electron microscopy (STEM) observation was performed using a focused ion beam DA300 system from FEI. TEM images were taken on the cross-section microstructure of the coatings using a Tecnai X-TWIN system from FEI, working at 200 kV. The dark field STEM images were taken using a Fischione high angle annular dark field detector. The chemical composition was measured by energy dispersive X-ray spectroscopy (EDX) analysis together with STEM imaging. Full quantification EDX analysis was performed using TEM Imaging and Analysis software.

HRTEM imaging was used to identify the misfit dislocation between the layers in the multilayer coating based on fast Fourier transformation (FFT) and geometric phase analysis (GPA). FFT and GPA of the high resolution micrographs were analyzed with Digital Micrograph software (version 3.11.1 Gatan). Bragg filtered image is generated by applying a spot mask to spots in the FFT of the HRTEM images. Afterwards, the FFT image was inverse Fourier filtered.

In order to characterize the thermal conductivity and thermal diffusivity of the coatings, the PPR method was used. First, a 1.0 μm thick gold film was deposited on the surface of the samples to enhance thermal absorption. A Nd-YAG laser (532 nm), operated in pulsed mode, with 7 ns full width at half maximum pulse duration, spot size (diameter of the laser beam on the gold layer) of 3 mm and pulse energy of 5 mJ was used to strike the sample and induce a temperature change at the surface of the samples. A 1 mW HeNe laser with 632.8 nm wavelength focused at the center of the pump spot with a 20 μm spot size to monitor

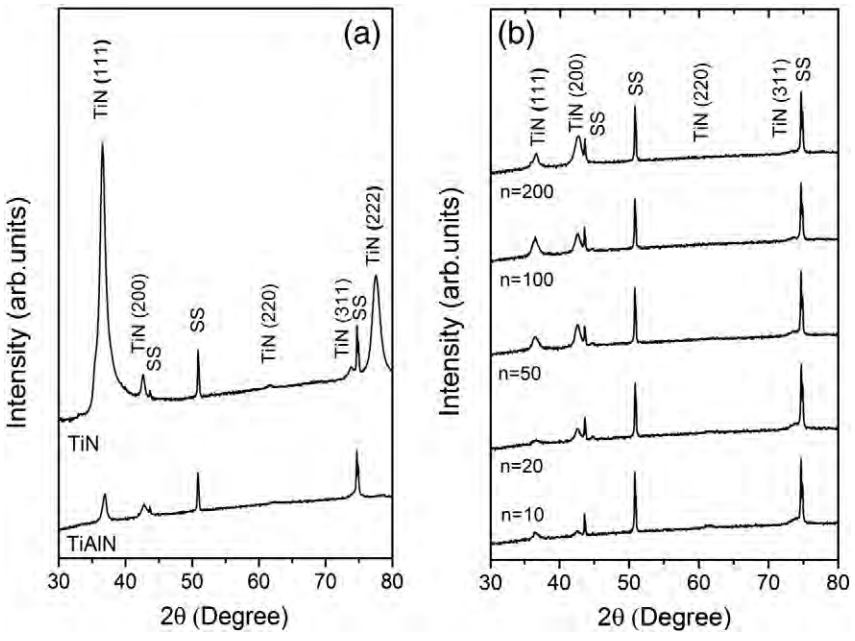

Fig. 1. X-ray diffraction pattern of the as-deposited (a) TiN and TiAlN single layer coatings and (b) $[TiN/TiAlN]_n$ multilayer coatings with different bilayer numbers *n*.

the changes in the beam reflected from the gold surface using a photodiode connected to a 125 MHz pre-amplifier. The temperature excursion of the metal surface $e(r,z,t)$ (i.e., the temperature rise above the ambient temperature T_0, as a function of the vertical direction z, the radial direction r, and time t) is measured through the temperature dependence of the metal's reflectivity. Since for most metals the thermoreflectance coefficient is about constant [16], the intensity of the reflected probe beam is inversely proportional to the gold surface temperature. By capturing the intensity profile of the reflected probe beam, the surface temperature excursion profile can be obtained and the relaxation rate of the profile is dependent on the thermal properties and thermal resistance of the underlying layers.

Because the effective thermal diffusion length and the spot size of the probe beam are much smaller than the spot size of the excitation beam, the measurement can be completed before any significant lateral heat diffusion occurs [14]. Therefore, the heat conduction problem can be modeled as one dimensional vertical heat diffusion in the three-layer (Au/$[TiN/TiAlN]_n$ multilayer/AISI 304) structure.

3. Results and analysis

Table 1 shows the EDX values of the Ti and Al content in the TiN and TiAlN layers in the multilayer coatings deposited with the LARC system with a bias voltage of −70 V at 480 °C. In order to measure the Ti and Al content in the multilayer stack (TiN and TiAlN layers), an EDX line scan analysis with 1 nm step size was performed along the vertical direction. Then the atomic ratio data were averaged in each layer. Fig. 1(a) shows the XRD patterns of the TiN and TiAlN single layer coatings deposited on AISI 304. The Al to Ti atomic ratio in the TiAlN coating is about 1.50. The diffraction peaks indicate that the TiN and TiAlN coatings were crystallized into a rocksalt-type cubic structure with the two strong Bragg peaks corresponding to the (111) plane (including the second order peak (222) for TiN), showing a preferential orientation growth along these orientations [17]. Ikeda et al. [18] studied the microstructure of TiN and TiAlN using XRD analysis and they reported also that with addition of Al to the TiN structure, the lattice parameter of the TiN coating monotonically decreases with increasing amount of Al atoms.

Fig. 1(b) shows the XRD patterns of the $[TiN/TiAlN]_n$ multilayer coatings deposited on AISI 304 with different bilayer number of 5, 10, 25, 50 and 100. The XRD patterns show a fcc structure of the coatings with two peaks at (111) and (200) corresponding to the TiN (111) and (200) planes. The intensity of the peaks in multilayer coatings is lower than the intensity of the peaks in the TiN single layer.

Fig. 2(a) shows a TEM cross-sectional image of as deposited single layer TiN deposited on AISI 304 by the LARC system. A columnar structure of TiN is clearly observed in the TEM image with a grain size of around 110 nm in width. A TEM cross-sectional image of an as deposited $[TiN/TiAlN]_{100}$ multilayer is shown in Fig. 2(b) as well. The periodic dark and bright layers in the TEM images are the TiN and TiAlN layers, respectively. Because of the lower scattering factor of Al, the TiAlN layer appears slightly brighter than the TiN layer [19]. The image displays the polycrystalline layers with columnar grains that grew through the multilayer cross section with around 50 nm wide columns.

Fig. 3(a) shows a HRTEM image of the $[TiN/TiAlN]_{100}$ multilayer coating along the <110> zone axis and the corresponding FFT in the inset. A magnified and IFFT filtered image of the region indicated by the white square in Fig. 3(a) is shown in Fig. 3(b). The FFT pattern reveals the fcc crystalline structure of the multilayer coating. GPA analysis was also carried out on the region indicated by dashed lines in Fig. 3(b), as shown in Fig. 3(c). The corresponding IFFT image of one family of planes is presented in Fig. 3(d). The dislocation can be clearly recognized as extra half planes which are indicated by "T" symbols. The misfit dislocations are shown along the interface in both the GPA map and IFFT image. The misfit dislocations form because of the lattice mismatch between the TiN and TiAlN layers and the Al content in the TiAlN layer, respectively. Suzuki et al. [20] reported that the lattice mismatch between

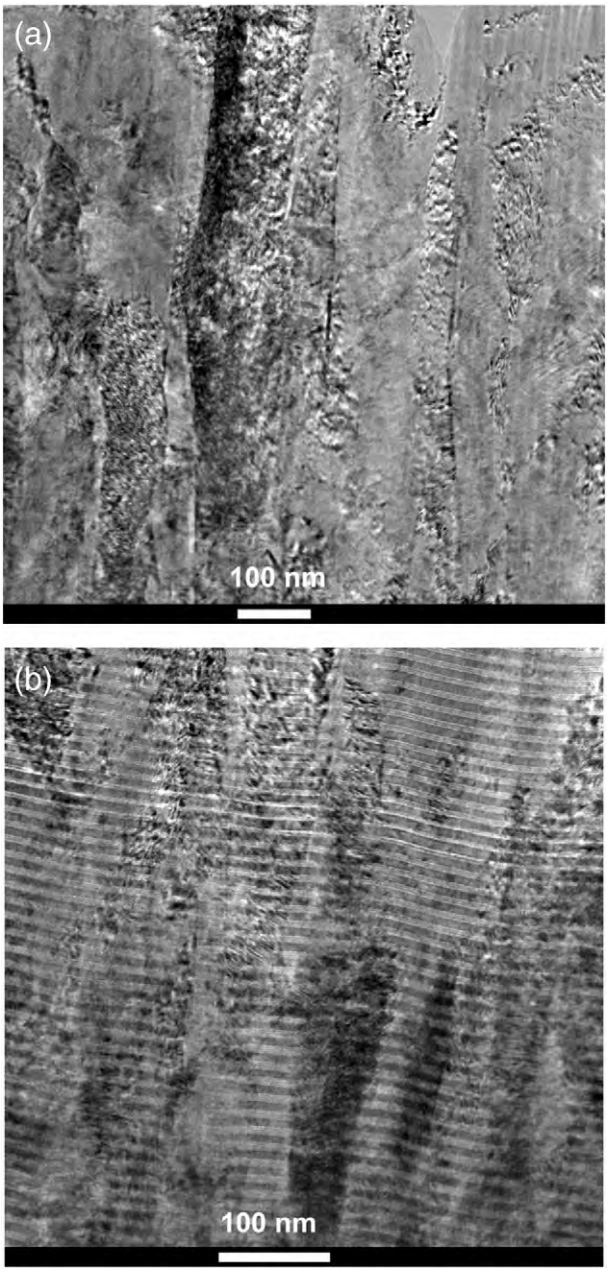

Fig. 2. Cross-sectional TEM images of (a) as-deposited TiN and (b) a $[TiN/TiAlN]_{100}$ multilayer deposited on AISI 304 substrate by the LARC system.

the TiN and TiAlN (with Al/Ti atomic ratio of about 1.0) coatings deposited by the cathode arc technique is about 1.4%. Fig. 4 shows a cross sectional STEM of as deposited $[TiN/TiAlN]_5$ and $[TiN/TiAlN]_{100}$ multilayer coatings. It can be observed that the columnar grain size reduces in width and in length by increasing the number of layers.

The normalized surface temperature profiles for the Au/$[TiN/TiAlN]_n$/AISI 304 structure with two different bilayer numbers 5 and 100 are shown in Fig. 5. In order to obtain the thermal conductivity and diffusivity of multilayer coatings, the temperature profile was fitted by a three layer heat conduction model, described in our previous works [21–23]. In the curve fitting process, three parameters (i.e., the thermal conductivity of the gold and $[TiN/TiAlN]_n$ multilayer coatings, and the thermal diffusivity of $[TiN/TiAlN]_n$ multilayer coatings) were varied and a least square optimization method was applied to minimize the difference between the normalized surface temperature profile and

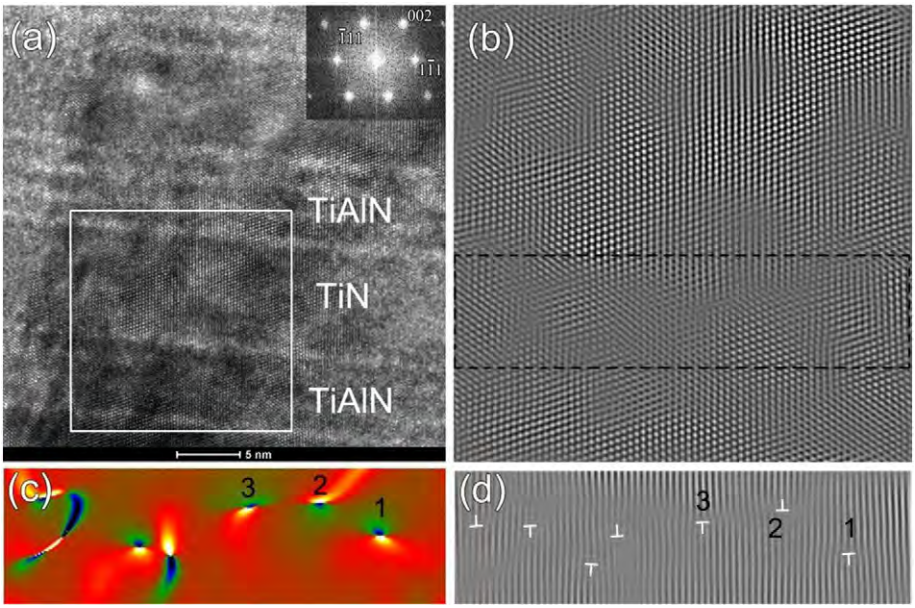

Fig. 3. (a) High resolution TEM image of a $[TiN/TiAlN]_{100}$ multilayer coating along the <110> direction. The corresponding fast Fourier transform (FFT) is shown in the upper right inset showing the fcc structure. (b) Magnified and inverse FFT of the region indicated by solid lines in (a) showing the atomic arrangement along the interface. (c) GPA map of the region indicated by the black dashed lines in (b) showing the position of the misfit dislocations at the interface as hot spots. (d) Inverse FFT of one family of planes to show the existence of dislocations indicated as extra half planes. Dislocations are shown by "T" symbols.

the three-layer model. The obtained average thermal conductivity for the gold film is 253 W/mK.

Fig. 6 displays the thermal conductivity of as deposited $[TiN/TiAlN]_n$ multilayer coatings as a function of the bilayer number. The thermal conductivity values of TiN and TiAlN single layer coatings are shown in the graph as well. It is observed that the thermal conductivity of TiN decreases rapidly with incorporation of Al in the TiN structure. The obtained thermal conductivity of the $[TiN/TiAlN]_5$ multilayer coating is 4.92 W/mK and the thermal conductivity decreases to 3.25 W/mK for the coating with bilayer number of 100. The thermal diffusivities of the TiN and TiAlN single layers and $[TiN/TiAlN]_n$ multilayer coatings as a function of the bilayer number are shown in Fig. 7. A similar behavior is observed for the thermal diffusivity, i.e., it decreases with increasing bilayer number.

4. Discussion

The dominant heat carriers in non-metallic crystalline solids are phonons. The mean free path of a phonon (MFP) is proportional to the thermal conductivity of materials based on kinetic theory [24]. Phonons scatter by impurities, dislocations, defects, and boundaries in the crystal lattice and phonon scattering determines the MFP. Impurity atoms, which can be introduced in the form of an alloy, in the lattice will change the acoustic impedance $Z = \rho v$, where ρ is the density and v is the speed of sound. Note that the speed of sound depends on the elastic stiffness of the chemical bond. When the incident phonon meets a change in the acoustic impedance, it will scatter and this leads to a lower thermal conductivity.

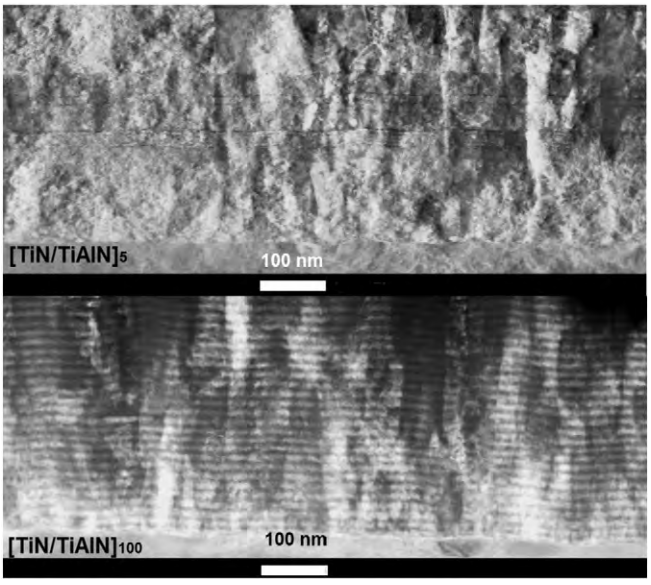

Fig. 4. Scanning cross sectional TEM images of multilayer $[TiN/TiAlN]_n$ coatings on AISI 304 substrate for a bilayer number n equal to 5 (top) and to 100 (bottom).

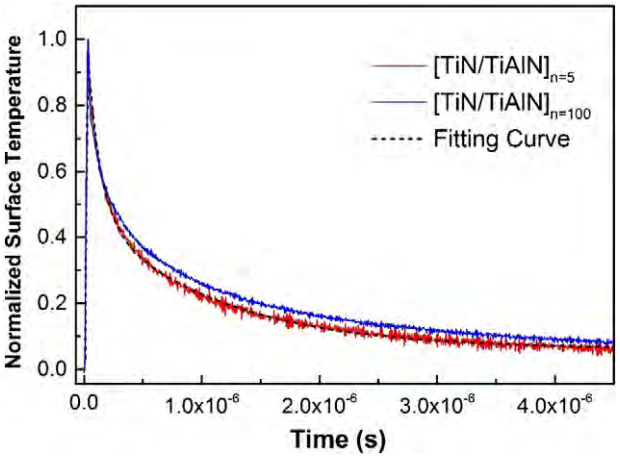

Fig. 5. Normalized surface temperature excursion profile of the as-deposited $[TiN/TiAlN]_n$ multilayer coatings with bilayer numbers $n = 5$ and $n = 100$.

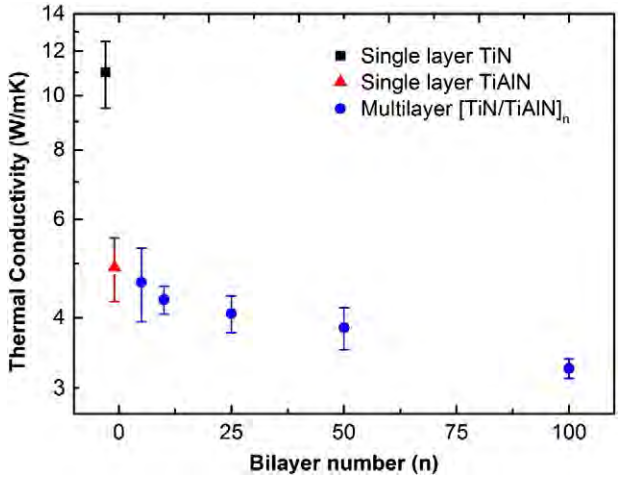

Fig. 6. Thermal conductivity of the as-deposited TiN, TiAlN single layers and $[TiN/TiAlN]_n$ multilayer coatings on AISI 304 substrate with different bilayers.

The effective thermal conductivity of multilayer coatings is determined by the thermal conductivity of each layer and the thermal boundary resistance between the layers. Defects such as misfit dislocations are formed between the layers when there is a mismatch between the lattice constants of the layers. Phonons are scattered by defects in interfaces between the layers, resulting in a reduced thermal conductivity. It was reported that the thermal conductivity of a multilayer film can be smaller than that of their alloys and decreases with increasing number of layers [25,26].

The XRD analysis shows that the microstructure of the TiN and TiAlN coatings strongly depends on the Al content. TiN shows a strong (111) diffraction peak with preferential orientation growth. TiN has a columnar structure as shown in Fig. 2(a) and this structure is very favorable to transfer heat in the cross-plane direction. The columnar structure and large grain size are responsible for the high thermal conductivity. With incorporation of Al into the TiN fcc structure, the intensity of the (111) peak reduces suddenly and the preferential orientation is disrupted. A previous study on the effect of incorporation of Al in the TiN structure demonstrated that Al is preventing the formation of the columns [27], resulting in a finer nanocrystalline structure. When the grain size of the coating is of the same order as the MFP, the grain boundaries play an important role to determine the thermal conductivity [28]. For smaller grain size of TiAlN, both the MFP and the thermal conductivity of the fine-grained TiAlN coatings drastically decrease [13].

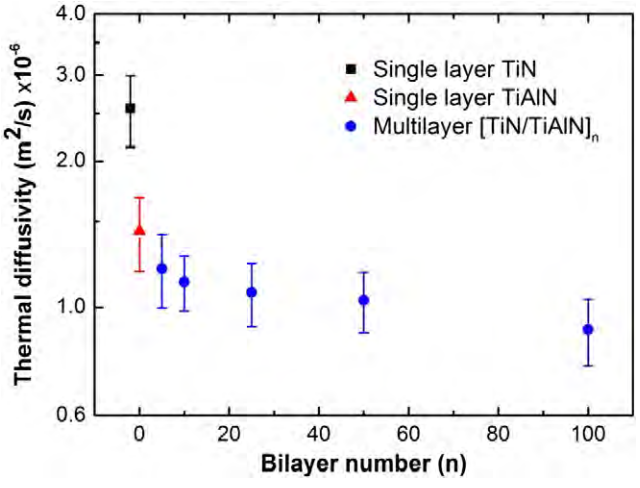

Fig. 7. Thermal diffusivity of the as-deposited TiN, TiAlN single layers and $[TiN/TiAlN]_n$ multilayer coatings with different bilayer numbers on AISI 304 substrate.

The (111) diffraction peak is weakened in multilayer coatings, such that the preferential orientation growth reduces in these coatings. HRTEM imaging and GPA were applied to examine the quality of the interfaces between the layers. Misfit dislocations are formed in the interfaces between the TiN and TiAlN layers because of strain energy due to lattice-mismatched multilayer growth [29,30]. By increasing the number of layers, the misfit dislocation density increases in the multilayer coating and phonon scattering increases at the interfaces of layers, resulting in a reduced thermal conductivity. The STEM observation of the two multilayer coatings with bilayer numbers of 5 and 100 confirmed that the columnar structure growth and grain size decrease with increasing number of layers. The multilayer deposition prevents the formation of the columns and results in a finer nanocrystalline structure. The phonon scattering increases in grain boundaries, and thus the MFP reduces, which results in a decreasing thermal conductivity of multilayer coatings. When increasing the bilayer number in the $[TiN/TiAlN]_n$ multilayer coatings, the decrease in thermal conductivity can be attributed to disruption of the columnar structure, and the increased phonon scattering at the interfaces of layers and grain boundaries.

5. Conclusion

A series of $[TiN/TiAlN]_n$ multilayer and a single layer TiN and TiAlN coatings were deposited on a stainless steel AISI 304 substrate by a lateral rotating cathode technique. The PPR technique was used to measure the cross-plane thermal conductivity of the coatings at room temperature. The obtained thermal conductivity for single layer TiN and TiAlN shows that the incorporation of Al in the TiN structure reduces the thermal conductivity significantly. XRD analysis and TEM imaging reveals that the preferential orientation growth along the (111) direction reduces in the coatings and that the grain size decreases with increasing the bilayer number. The HRTEM images and GPA maps of multilayer coatings show extensive defects at the interfaces between the TiN and TiAlN layers because of strain energy due to lattice-mismatched multilayer growth. The decrease in grain size and increase in misfit dislocation density in the multilayer coating are responsible for reducing heat transport in the coatings with increasing bilayer number.

References

[1] W.D. Munz, Titanium aluminum nitride films: a new alternative to TiN coatings, J. Vac. Sci. Technol. A 4 (1986) 2717.
[2] J. Musil, H. Hrubý, Superhard nanocomposite TiAlN films prepared by magnetron sputtering, Thin Solid Films 365 (2000) 104.
[3] X.Z. Ding, C.T. Bui, X.T. Zeng, Abrasive wear resistance of Ti1 − xAlxN hard coatings deposited by a vacuum arc system with lateral rotating cathodes, Surf. Coat. Technol. 203 (2008) 680.
[4] S. PalDey, S. Deevi, Properties of single layer and gradient (Ti, Al) N coatings, Mater. Sci. Eng. A 361 (2003) 1.
[5] A. Knutsson, M.P. Johansson, L. Karlsson, M. Odén, Thermally enhanced mechanical properties of arc evaporated Ti 0.34Al 0.66 N/TiN multilayer coatings, J. Appl. Phys. 108 (2010) 044312.
[6] S. PalDey, S.C. Deevi, Single layer and multilayer wear resistant coatings of (Ti, Al)N: a review, Mater. Sci. Eng. A 342 (2003) 58.
[7] S.M. Lee, H.M. Chow, F.Y. Huang, B.H. Yan, Friction drilling of austenitic stainless steel by uncoated and PVD AlCrN-and TiAlN-coated tungsten carbide tools, Int. J. Mach. Tools Manuf. 49 (2009) 81.
[8] N. Abukhshim, P. Mativenga, M. Sheikh, Heat generation and temperature prediction in metal cutting: a review and implications for high speed machining, Int. J. Mach. Tools Manuf. 46 (2006) 782.
[9] W. Kalss, A. Reiter, V. Derflinger, C. Gey, J.L. Endrino, Modern coatings in high performance cutting applications, Int. J. Refract. Met. Hard Mater. 24 (2006) 399.
[10] E. Lugscheider, H. Geiler, M. Lake, H. Zimmermann, Investigation of thermophysical properties of AIP coated cutting tools for dry machining, Surf. Coat. Technol. 86 (1996) 803.
[11] D.G. Cahill, S.-M. Lee, T.I. Selinder, Thermal conductivity of κ-Al 2 O 3 and α-Al 2 O 3 wear-resistant coatings, J. Appl. Phys. 83 (1998) 5783.

[12] G.S. Fox-Rabinovich, K. Yamamoto, M.H. Aguirre, D.G. Cahill, S.C. Veldhuis, A. Biksa, G. Dosbaeva, L.S. Shuster, Multi-functional nano-multilayered AlTiN/Cu PVD coating for machining of Inconel 718 superalloy, Surf. Coat. Technol. 204 (2010) 2465.
[13] X.Z. Ding, M.K. Samani, G. Chen, Thermal conductivity of PVD TiAlN films using pulsed photothermal reflectance technique, Appl. Phys. A Mater. Sci. Process. 101 (2010) 573.
[14] M.K. Samani, X. Ding, S. Amini, N. Khosravian, J. Cheong, G. Chen, B. Tay, Thermal conductivity of titanium aluminum silicon nitride coatings deposited by lateral rotating cathode arc, Thin Solid Films 537 (2013) 108.
[15] X.Z. Ding, A.L.K. Tan, X.T. Zeng, C. Wang, T. Yue, C.Q. Sun, Corrosion resistance of CrAlN and TiAlN coatings deposited by lateral rotating cathode arc, Thin Solid Films 516 (2008) 5716.
[16] K. Ujihara, Reflectivity of metals at high temperatures, J. Appl. Phys. 453 (1972) 2376.
[17] B. Tay, X. Shi, H. Yang, H. Tan, D. Chua, S. Teo, The effect of deposition conditions on the properties of TiN thin films prepared by filtered cathodic vacuum-arc technique, Surf. Coat. Technol. 111 (1999) 229.
[18] T. Ikeda, H. Satoh, Phase formation and characterization of hard coatings in the Ti1 − *x* AlxN system prepared by the cathodic arc ion plating method, Thin Solid Films 195 (1991) 99.
[19] A. Madan, I. Kim, S. Cheng, P. Yashar, V. Dravid, S. Barnett, Stabilization of cubic AlN in epitaxial AlN/TiN superlattices, Phys. Rev. Lett. 78 (1997) 1743.
[20] T. Suzuki, D. Huang, Y. Ikuhara, Microstructures and grain boundaries of (Ti, Al) N films, Surf. Coat. Technol. 107 (1998) 41.
[21] M.K. Samani, N. Khosravian, G.C.K. Chen, M. Shakerzadeh, D. Baillargeat, B.K. Tay, Thermal conductivity of individual multiwalled carbon nanotubes, Int. J. Therm. Sci. 62 (2012) 40.
[22] M. Shakerzadeh, M. Samani, N. Khosravian, E. Teo, M. Bosman, B. Tay, Thermal conductivity of nanocrystalline carbon films studied by pulsed photothermal reflectance, Carbon 50 (2012) 1428.
[23] G. Chen, P. Hui, Pulsed photothermal modeling of composite samples based on transmission-line theory of heat conduction, Thin Solid Films 339 (1999) 58.
[24] C. Kittel, P. McEuen, Introduction to Solid State Physics, Wiley, New York, 1976.
[25] Z. Zhang, J. Roger, D. Fournier, A. Boccara, J. Wang, Thermal diffusivity of amorphous semiconductor superlattice films, Thin Solid Films 186 (1990) 361.
[26] S.M. Lee, D.G. Cahill, R. Venkatasubramanian, Thermal conductivity of Si–Ge superlattices, Appl. Phys. Lett. 70 (1997) 2957.
[27] S.H. Lee, J.J. Lee, Compositionally gradient (Ti 1 − *x*Al*x* N coatings made by plasma enhanced chemical vapor deposition, J. Vac. Sci. Technol. A 13 (1995) 2030.
[28] J.R. Nicholls, K.J. Lawson, A. Johnstone, D.S. Rickerby, Methods to reduce the thermal conductivity of EB-PVD TBCs, Surf. Coat. Technol. 151–152 (2002) 383.
[29] J. Matthews, A. Blakeslee, Defects in epitaxial multilayers: I. Misfit dislocations, J. Cryst. Growth 27 (1974) 118.
[30] L. Freund, The stability of a dislocation threading a strained layer on a substrate, J. Appl. Mech. 54 (1987) 553.